

C-band 160 Gbs⁻¹ Zero-bias Graphene Photodetectors: Breaking the Responsivity–Bandwidth Trade-off by Heterostructure Engineering

Karuppasamy Pandian Soundarapandian^{*1}, Alberto Montanaro^{†2,3}, Ioannis Vangelidis^{†6}, Stefan M. Koepfli⁷, Lorenzo Orsini¹, Matteo Ceccanti¹, Laurenz Kulmer⁷, Misal Misal², Tom Reep⁸, Sebastián Castilla¹, Kenji Watanabe⁹, Takashi Taniguchi¹⁰, Seth Ariel Tongay¹¹, Dries Van Thourhout⁸, Juerg Leuthold⁷, Klaas-Jan Tielrooij^{12,13}, Elefterios Lidorikis^{6,14}, Marco Romagnoli^{‡2,4}, Vito Soriano^{‡2,5}, and Frank H. L. Koppens^{*1}

¹ICFO – Institut de Ciències Fotòniques, The Barcelona Institute of Science and Technology, 08860 Castelldefels (Barcelona), Spain

²CNIT – National Inter-University Consortium for Telecommunications, 56127 Pisa, Italy

³TeCIP Institute, Scuola Superiore Sant’Anna, 56124, Pisa, Italy

⁴2D Photonics spa, 20900, Monza (MB), Italy

⁵Camgraphic srl, 20900, Monza (MB), Italy

⁶Department of Materials Science and Engineering, University of Ioannina, Ioannina, Greece

⁷ETH Zurich, Institute of Electromagnetic Fields (IEF), Zurich, Switzerland

⁸Department of Information Technology (INTEC), Ghent University—IMEC, Ghent, Belgium

⁹National Institute for Materials Science (NIMS), Tsukuba, Japan

¹⁰Research Center for Materials Nanoarchitectonics, NIMS, Tsukuba, Japan

¹¹Arizona State University, Tempe, Arizona, USA

¹²Catalan Institute of Nanoscience and Nanotechnology (ICN2), CSIC and BIST, Barcelona, Spain

¹³Department of Applied Physics, TU Eindhoven, Eindhoven, Netherlands

¹⁴University Research Center of Ioannina (URCI), Institute of Materials Science and Computing, Ioannina, Greece

Abstract

Graphene photodetectors offer ultrafast response and broadband operation, but their responsivity is typically limited by rapid hot-carrier cooling, leading to a trade-off between sensitivity and speed. Here, we demonstrate that modifying the dielectric environment provides an effective route to control hot-carrier cooling and enhance device performance. By employing a WSe₂ encapsulation architecture, we suppress out-of-plane energy dissipation, leading to an increased cooling length ($\sim 2.68 \mu\text{m}$) and a reduced heat-exchange coefficient β . As a result, we obtain zero-bias graphene photodetectors with responsivities up to $\sim 0.12 \text{ A/W}$ (Potentially $\sim 0.4 \text{ A/W}$) while maintaining ultrafast operation beyond setup limited 110 GHz. The devices enable direct detection at data rates of 120 Gb s^{-1} (NRZ) and 160 Gb s^{-1} (PAM-4), with performance achieved using minimal digital signal processing. These results establish dielectric engineering as a key design axis for controlling hot-carrier dynamics, enabling energy-efficient, high-speed optical receivers for next-generation interconnects and AI-driven data systems.

Introduction

The exponential growth in global data traffic requires low-cost, energy-efficient, high-bandwidth integrated photonic devices capable of sustaining the persistent increase in data rate demands^{1–3}. With the 1.6 Tbs⁻¹ Ethernet standard under development⁴, photodetectors (PDs) that support simple modulation formats at ultra-high bandwidths are critical for reducing reliance on complex digital signal processing (DSP)^{5–7}. The incumbent Ge-on-Si platform achieves responsivities of 0.3–1.0 A/W at bandwidths up to 265 GHz⁸, with recent Ge-fin architectures

[†]These authors contributed equally to this work.

[‡]the work has been performed while employed at CNIT, PNTLab

*Corresponding author: karuppasamy.soundarapandian@icfo.eu, frank.koppens@icfo.eu

on scalable silicon photonic platforms reaching 240–265 GHz at 0.3 A/W⁸, and co-integrated GeSi-fin photodiodes exceeding 200 GHz in monolithic platforms⁹. III–V InP-based modified uni-travelling-carrier (MUTC) photodiodes reach 0.16–0.24 A/W at bandwidths exceeding 220 GHz^{10,11}; however, they require heterogeneous integration with silicon photonics via transfer-printing of III–V coupons, which increases fabrication complexity at scale¹². Critically, both technologies require reverse bias and a transimpedance amplifier (TIA) to convert photocurrent into a usable voltage—a component that dominates receiver power consumption and circuit complexity in massively parallel optical interconnects. In this context, graphene has emerged as a compelling alternative, combining single-layer thickness^{13,14}, ultrabroadband absorption^{15–17}, high carrier mobility¹⁸, and complementary metal-oxide-semiconductor (CMOS) back-end-of-line (BEOL) compatibility¹⁹ to enable on-chip PDs spanning all telecom bands (O, E, S, C, L, and U)^{20–22}. To date, graphene-based PDs have demonstrated responsivities up to ~ 0.7 A/W^{23–28} and bandwidths up to 500 GHz^{25,26,29} by exploiting bolometric^{23,26} and photoconductive²⁷ effects. These devices, however, operate under applied bias, resulting in substantial dark current and correspondingly high energy consumption^{26–28}.

Conversely, the photothermal effect (PTE) and photovoltaic effect do not require any bias and thus exhibit near-zero dark current. The PTE effect generates a photovoltage from the spatially varying temperature profile³⁰, and PTE-based graphene-integrated PDs (GIPDs) have reached up to 6 V/W responsivity, 110 GHz bandwidth, and 120 Gbs⁻¹ data rates^{24,26,31–36}. This performance was driven by efforts to enhance the Seebeck coefficient (S) by improving the quality of graphene. On the other hand, plasmonic structures and ring resonators enhance ∇T_e through improved absorption³⁷ and achieve responsivities up to 12.2 V/W and 90 V/W. However, their bandwidths are limited to 42 GHz and 12 GHz, respectively^{35,38}. These approaches also present significant drawbacks: (i) plasmonic resonances typically require sub-100 nm lithographic features, making the platform less scalable and highly sensitive to fabrication tolerances, as even minor misalignments can lead to high optical losses or reduced plasmonic enhancement³⁹; (ii) ring resonators inherently limit the bandwidth of the device, as defined by the optical bandwidth of the ring resonator³⁵. Therefore, a trade-off exists between responsivity and bandwidth^{40–42}. Despite extensive work on mobility and absorption, dielectric-environment control of hot-carrier cooling remains largely unexplored in graphene photodetectors.

In principle, enhancing the S or optical absorption alone does not overcome the intrinsic thermal limitation of the PTE effect. In high-quality graphene (i.e. mobility $> 15,000$ cm²V⁻¹s⁻¹), the S saturates and becomes largely insensitive to further improvements in material quality, making it ineffective for further enhancing responsivity. Importantly, this does not imply that higher mobility is detrimental in general; rather, in the PTE regime, increased mobility enhances thermal conductivity, which accelerates hot-carrier cooling and reduces the electron temperature gradient (∇T_e) driving the photoresponse. As a result, device performance is governed by the generalized heat-exchange coefficient, $\beta = \sqrt{c_e \kappa_e / \tau_c}$, which incorporates both thermal conductivity κ_e and the cooling time of hot carriers τ_c .

Here, we demonstrate that engineering hot-carrier cooling, rather than maximizing carrier mobility, is key to improving zero-bias graphene PDs without compromising bandwidth. We achieve this through an encapsulation-driven strategy that enhances graphene-PD responsivity by engineering β via reduced thermal conductivity and prolonged cooling times. Notably, this method does not rely on resonant structures, thereby preserving fabrication simplicity and the intrinsic ultrafast response of graphene. To implement this strategy, we employ tungsten diselenide (WSe₂) as both the top and bottom encapsulant (WSe₂/Gr/WSe₂ - Type 2) in a waveguide-integrated architecture, enabling efficient photovoltage generation via the PTE effect. The effects of WSe₂ encapsulation on the electronic and optoelectronic properties of graphene are presented through systematic analysis. We observed that the room-temperature mobility of (WSe₂/Gr/hBN) Type 1 heterostructures were higher than the others types reported. We then measured the cooling length (ξ) of ~ 2.68 μm for the Type 2 heterostructure, almost double that of the Type 1. These contrasting behaviours directly influence photodetector performance since β governs the responsivity. Accordingly, we fabricated Type 1 and Type 2 waveguide-integrated PDs, which exhibited responsivities exceeding 0.045 A/W and 0.12 A/W, respectively, with no observable roll-off in the frequency response up to 110 GHz at 1550 nm (measurement-limited), consistent with the proposed mechanism. By combining high responsivity and bandwidth, these PDs achieved setup-limited direct detection of non-return-to-zero (NRZ) and PAM-4 optical signals at data rates of 120 and 160 Gbs⁻¹, respectively. These findings, together with the developed theoretical model, refine the conventional expectation that higher material quality alone enhances responsivity, by highlighting the competing role of hot-carrier cooling.

Results

Transport characterisation

Fig. 1a presents a schematic of the waveguide-integrated graphene photodetector used in this work, with the inset highlighting the heterostructures employed, in particular the channel stack. This structural detail is critical, as the responsivity is governed by β , which captures the interplay between thermal conductivity and cooling dynamics³⁷.

Because the thermal conductivity is directly proportional to carrier mobility, the choice of encapsulating materials in the graphene heterostructure plays a central role in device performance. State-of-the-art graphene encapsulation with hBN is the most common and experimentally accessible strategy for enhancing carrier mobility to values exceeding $150,000 \text{ cm}^2\text{V}^{-1}\text{s}^{-1}$ ⁴³⁻⁴⁵, thereby enabling S as high as $\sim 300 \mu\text{V}/\text{K}$ ³⁵. However, the S saturates for mobilities beyond $\sim 10,000 \text{ cm}^2\text{V}^{-1}\text{s}^{-1}$, such that further increases in mobility predominantly enhance thermal conductivity and, consequently, reduce responsivity^{31,37}. Concurrently, the residual carrier density (n^*) becomes a limiting factor. An optimal regime combines moderately high mobility with low n^* , providing favourable conditions for efficient photodetection. Mobility and disorder must be balanced rather than maximizing mobility alone. Therefore, to address the aforementioned limitations, we propose WSe₂ as an alternative, an atomically flat and potentially scalable 2D material that exhibits weaker hot-carrier-phonon coupling than hBN⁴⁶.

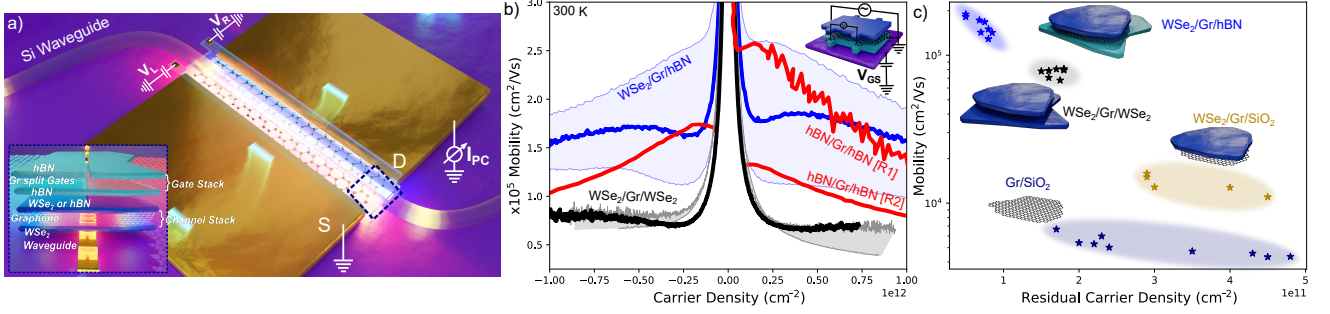


Figure 1: Heterostructure-dependent electrical quality in graphene. **a** Schematic of the waveguide-integrated graphene photodetector, with inset showing the van der Waals heterostructure stack. **b** Carrier mobility for graphene encapsulated Hall-bars with different encapsulants, demonstrating significant variation depending on the heterostructure. The shaded region represents the device-to-device variation range between the minimum and maximum measured value. **c** Residual charge density (n^*) as a function of mobility, establishing the relationship between the mobility and n^* for different heterostructures

First, we examined the influence of WSe₂ encapsulation on graphene mobility. To do so, we fabricated heterostructures with three distinct configurations: WSe₂/Gr/hBN (Type 1), WSe₂/Gr/WSe₂ (Type 2), and WSe₂/Gr/SiO₂. Subsequently, these heterostructures were fabricated into Hall-bar geometries for four-terminal transport measurements, as shown in the inset of Fig. 1b. Fig. 1b shows the measured Drude mobility ($\mu = \sigma/(ne)$) as a function of the charge carrier density (n) induced by the gate voltage, where Types 1 and 2 are compared with the state-of-the-art reference hBN/Gr/hBN heterostructures R1⁴⁵ and R2⁴³. Type 1 devices exhibited an average mobility of $\sim 155,000 \text{ cm}^2\text{V}^{-1}\text{s}^{-1}$ for both the electron and hole transport at $n \approx 1 \times 10^{12} \text{ cm}^{-2}$ at room temperature. This exceeds the performance of R1 and R2, highlighting the effectiveness of WSe₂ as a capping layer. In contrast, Type 2 devices exhibited a lower value of $\sim 80,000 \text{ cm}^2\text{V}^{-1}\text{s}^{-1}$ at $n \approx 1 \times 10^{12} \text{ cm}^{-2}$. The blue and grey shaded regions in the plot indicate the mobility ranges measured across different devices of Types 1 and 2 heterostructures.

Next, in Fig. 1c, we compared the n^* values of Types 1, 2, and 3 with those of a standard Gr/SiO₂ device to evaluate the disorder introduced by WSe₂ encapsulation. The mobility values presented here were measured at $n = 1 \times 10^{12} \text{ cm}^{-2}$. The n^* value was estimated by identifying the intersection point between the linear and flat regions of the n -dependent conductivity curve. As anticipated, the Gr/SiO₂ device exhibited a high n^* in the range of approximately $1.5\text{-}5 \times 10^{11} \text{ cm}^{-2}$. However, capping graphene with WSe₂ (Type 3) resulted in a comparable n^* range while achieving twice the mobility. Type 2 devices exhibited a more uniform n^* in the narrow range of $1.5\text{-}1.8 \times 10^{11} \text{ cm}^{-2}$, achieving an approximately fivefold increase in mobility compared to Type 3 devices, clearly highlighting the influence of WSe₂ as a substrate. Nevertheless, Type 1 devices have the lowest n^* range of $\sim 5\text{-}9 \times 10^{10} \text{ cm}^{-2}$, indicating minimal induced disorder, leading to the highest mobility among all combinations. The observed relationship between the mobility and n^* aligns with the literature^{47,48} and explains the mobility variations depicted for Types 1 and 2 in Fig. 1b. As an atomically flat substrate, the n^* of Type 2 devices is expected to closely resemble that of Type 1 devices. The strain induced by the lattice mismatch ($\sim 25\%$)⁴⁹ may explain the observed differences; however, further studies are required, which lie beyond the scope of the present work.

Cooling length determination

Next, we focused on the thermal management of the hot carriers in the heterostructures discussed above, since $\Delta T_e \propto \frac{\sinh(\frac{W}{2\xi})}{2W \cosh(\frac{W}{2\xi})}$, with particular emphasis on the cooling length $\xi = \sqrt{\frac{\kappa_e}{\gamma c_e}}$, where W is the source-drain length, κ_e is the thermal conductivity of graphene, γ is the electron-lattice cooling rate, and c_e is the specific

heat capacity⁴⁰. Among the various hot-carrier cooling mechanisms, out-of-plane cooling through a substrate is the dominant process in high-quality graphene-based heterostructures (hBN/Gr/hBN). In particular, hyperbolic phonons in hBN-encapsulated devices play a crucial role in enabling efficient cooling⁵⁰. To measure the ξ for the Type 1 and Type 2 heterostructures, we first fabricated long-channel PDs (See Supp. Note 2) on top of the hBN/Gr bottom split gates and compared the results with those of an hBN/Gr/hBN heterostructure. The electrical and optoelectronic properties of the PDs were determined, and their mobilities, n^* , and operating gate voltage (OGV) were carefully extracted (See Supp. Note 3). These long-channel scattering-type scanning near-field optical microscopy (sSNOM) PDs are distinct from the Hall bars (Fig. 1) and the waveguide-integrated PDs (Fig. 3); the open-access channel geometry required by sSNOM probing is incompatible with the waveguide-integrated geometry (see Methods).

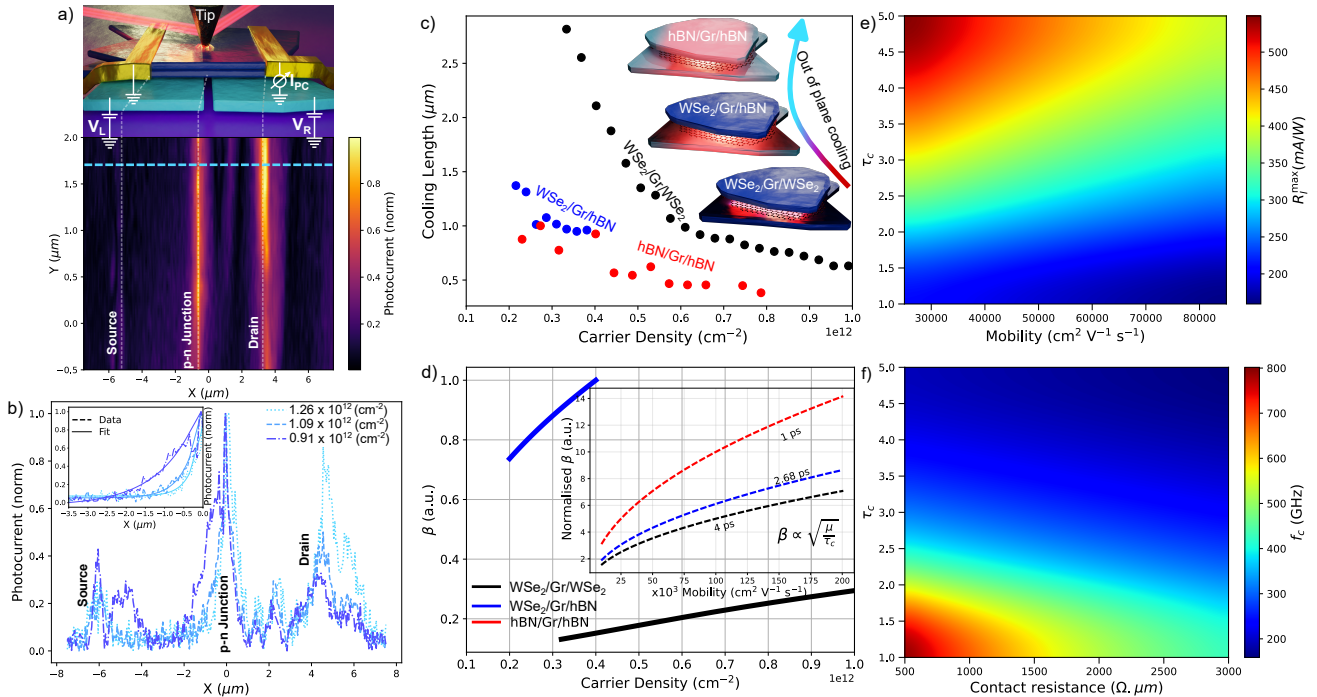


Figure 2: Cooling length characterisation in high-quality heterostructures. **a** Schematic of the sSNOM technique (top) and corresponding two-dimensional photocurrent map of the Type 2 heterostructure (bottom). The dashed lines indicate the linecuts used to extract the photocurrent profiles shown in Fig. 2b for different carrier densities (n). **b** Line profiles of the photocurrent for three carrier densities (n), extracted along the blue line in Fig. 2a; the inset shows a representative fit. **c** Extracted cooling length (ξ) as a function of n for three heterostructures (hBN/Gr/hBN, Type 1, Type 2); Type 2 exhibits a longer ξ , indicating suppressed hot-carrier cooling. Data points with carrier densities near the residual charge density (n^*) are excluded to avoid misleading interpretation near the charge inhomogeneity regime. The inset shows a schematic representation of out-of-plane cooling in the heterostructures. **d** Normalized heat exchange coefficient β calculated from the measured cooling length and the thermal conductivity of Type 1 (blue) and Type 2 (black) heterostructures, plotted against n . The inset shows the calculated β as a function of mobility for three cooling times 1 ps, 2.68 ps, and 4 ps corresponding to hBN/Gr/hBN, Type 1, and Type 2 heterostructures, respectively. **e** Analytical upper-bound responsivity $R_I^\infty = \frac{qS}{\beta}$ as a function of mobility μ and cooling time τ_c , evaluated using the closed-form framework (see Methods). **f** Simulated Bandwidth estimator $f_c = (f_{c1}^{-1} + f_{c2}^{-1})^{-1}$ as a function of contact resistance and cooling time, with $C = 2$ fF (see Methods).

The sSNOM tip serves as a near-field point source for localized illumination of the channel. Under illumination from a focused IR laser beam, the sSNOM tip exhibits the enhanced light-induced phenomenon known as the “lightning rod effect.” This effect generates a highly localized hotspot of light at the apex of the scanning tip^{51,52}. This technique enables spatially resolved photoresponse at the nanoscale. Fig. 2a (top) shows a schematic representation and measurement configuration of the fabricated devices. Gate voltages were applied to the bottom split gates to create a p-n junction. Spatial scans of the PDs were performed while measuring the resulting photocurrent, as shown in Fig. 2a (bottom). The map revealed three distinct regions of photoresponse corresponding to the graphene/metal interface and the p-n junction formed. This process identified a clean region for extracting ξ , as depicted by the dotted blue line in the photocurrent map. Next, we performed a gate-voltage-dependent line scan along the blue dotted line while simultaneously sweeping the split-gate voltage simultaneously, that is (left gate = right gate), the p-n and n-p regions of the PTE response, where the photocurrent is maximal. Fig. 2b presents the line cuts from the Type 2 device, acquired at $n = 0.91, 1.09, \text{ and } 1.25 \times 10^{12} \text{ cm}^{-2}$, respectively.

Increasing gate voltage enhances exponential decay near the p–n junction. This indicates a reduced cooling length ξ . The inset shows the exponential fit (solid line) obtained to extract the ξ from the gate-voltage-dependent line scans (dotted lines).

Fig. 2c shows the ξ of the Type 1, Type 2, and hBN/Gr/hBN PDs as a function of the n . The ξ , extracted from the gate-voltage-dependent line-scan maps (See Supp. Note 3), was $\sim 1 \mu\text{m}$, $\sim 1.4 \mu\text{m}$, and $\sim 2.68 \mu\text{m}$ for the hBN/Gr/hBN PDs, Type 1, and Type 2, respectively. Values of ξ below n^* were disregarded to ensure fair and practical consideration of the operational n of a PD. At higher carrier density, hot-carrier cooling and optical phonon cooling becomes more efficient, leading to shorter ξ ^{46,50}. hBN/Gr/hBN PDs exhibit the lowest ξ at even small n ; this is due to the stronger out-of-plane cooling of the hot carriers into hBN, aided by hyperbolic phonons⁵⁰. By contrast, Types 1 and 2 exhibit longer ξ , reflecting reduced heat-dissipation pathways (substrate phonon coupling) due to partial or complete removal of hBN encapsulation. The systematic increase in ξ observed across the heterostructures provides strong experimental evidence that dielectric environment governs hot-carrier cooling in graphene, consistent with previous studies^{46,50?}. Type 2 exhibits the longest cooling length among the reported graphene heterostructures^{30,50,53,54}. Suppressed coupling to substrate phonons shifts hot-carrier relaxation toward optical-phonon-mediated cooling, a process sustained by carrier–carrier scattering through rapid carrier re-thermalization⁴⁶. In the Type 2 heterostructure, the dielectric environment is expected to weaken carrier–carrier scattering, thereby reducing the efficiency of optical phonon emission and suppressing hot-carrier cooling as seen in recent studies^{55, Yishu et al., arXiv, 2026}.

The extracted cooling length outside the hydrodynamic heat-flow-dominated Dirac fluid regime⁵⁶, together with the measured conductivity of the heterostructures, was used to determine the cooling time (τ_c), yielding average values of ~ 1 ps, ~ 2.6 ps and ~ 4 ps for hBN/Gr/hBN, Type 1 and Type 2 around the OGV (See Supp. Note 1), respectively, consistent with the literature^{46,50}. To make the role of thermal transport explicit, β is estimated from the experimentally extracted ξ and the thermal conductivity inferred from σ , providing a physically consistent metric for comparing hot-carrier cooling across heterostructures (Fig. 2d). The Type 2 heterostructure exhibits a lower β across the operating range compared to Type 1. The inset illustrates the scaling of β with μ and τ_c , showing that the reduced β in Type 2 arises from its extended cooling dynamics despite lower mobility. Substituting the measured (μ, τ_c, n^*) of each stack into the contact-dominated scaling $R_I^\infty \propto \sqrt{\tau_c/\mu}$ established in the Introduction (with the contact-dominated regime $R_C \gg R_G$ verified experimentally in the DC characterization below), Type 2's longer τ_c outweighs its lower mobility, exactly the trade-off Type 2 wins over Type 1. Using the measured μ and extracted τ_c , we evaluated the analytical PD responsivity (See Supp. Note 1), thereby probing the upper limit of the responsivity in the engineered heterostructures as shown in Fig. 2e. Given the enhanced τ_c observed in these heterostructures and the dominance of contact resistance (R_c) over channel resistance in our devices, we evaluated the analytical frequency response (f_c) as a function of τ_c and R_c to estimate the achievable bandwidth. Fig. 2f was obtained by considering $f_c = (f_{c1}^{-1} + f_{c2}^{-1})^{-1}$, $f_{c1} = \frac{1}{2\pi R_D C}$, $f_{c2} = \frac{1}{\tau_c}$, with $R_D = R_G + R_C$ the total device resistance and $C = 6$ fF, consistent with previously measured devices and the literature^{36,37}. This, in turn, enables rational selection of channel length and width for the PD, subject to the constraint that the PD length should be $< \xi$ ⁵⁷. Simulations predict responsivities above 0.4 A/W at 250–300 GHz for Type 2 devices. Type 1 devices reach 0.3–0.4 A/W at 350–450 GHz. Thus, the systematic reduction of β across heterostructures, together with the concurrent increase in cooling length, provides direct experimental evidence that the dielectric environment, not carrier mobility alone, governs hot-carrier cooling, and thereby the resulting responsivity.

DC characterisation of the waveguide-integrated PD

Prior to device fabrication, the substrate and capping-layer thicknesses and the device dimensions were optimised by COMSOL simulations to maximise the optical absorption in graphene for both Type 1 and Type 2 (see Supp. Note 1). The source–drain distance was fixed at $W = 3 \mu\text{m}$ and the channel length along the waveguide at $L = 60 \mu\text{m}$, balancing channel resistance (which decreases with longer L) and the diminishing returns of the graphene absorption tail at large L . The silicon waveguide width is $w = 450$ nm, corresponding to a Gaussian optical-mode FWHM of $\sim 0.42 \mu\text{m}$ at the graphene level ($\sigma \approx 180$ nm). Fig. 3a shows the simulated TE-mode absorption profile yielding an overall $\alpha_{\text{SLG}} \approx 60\%$; the dotted rectangle outlines the waveguide/channel area.

We evaluated the fabricated split gates by measuring under 5 mV source-drain bias as a function of the two gate voltage V_{LG} , V_{RG} . The contour map in Fig. 3b shows the characteristic p–n pattern with a peak resistance of $\sim 112 \Omega$ at the charge-neutrality. From the resistance $R(V_G)$ along the symmetric line $V_{\text{LG}} = V_{\text{RG}}$ (Fig. 3c), we extracted two-terminal hole and electron mobilities using a model³² as $\sim 37,000 \text{ cm}^2\text{V}^{-1}\text{s}^{-1}$ and $\sim 43,000 \text{ cm}^2\text{V}^{-1}\text{s}^{-1}$, respectively, with an $n^* \sim 2.1 \times 10^{11} \text{ cm}^{-2}$ for the Type 2 PD - a lower bound on the channel mobility, owing to the contact-resistance contribution embedded in the two-terminal readout. The shape of $R(V_G)$ yields, via the Mott formula³⁰, a Seebeck coefficient $S \approx 300 \mu\text{V}/\text{K}$, consistent with Seebeck saturation at the high mobilities of our devices. Decomposing the two-terminal device resistance into channel and contact contributions yields the channel resistance $R_G \approx 15 \Omega$ and the contact resistance $R_C \approx 75 \Omega$ total at the OGV (ratio $R_C/R_G \approx 5$). The device therefore operates in the contact-resistance-dominated regime in which the

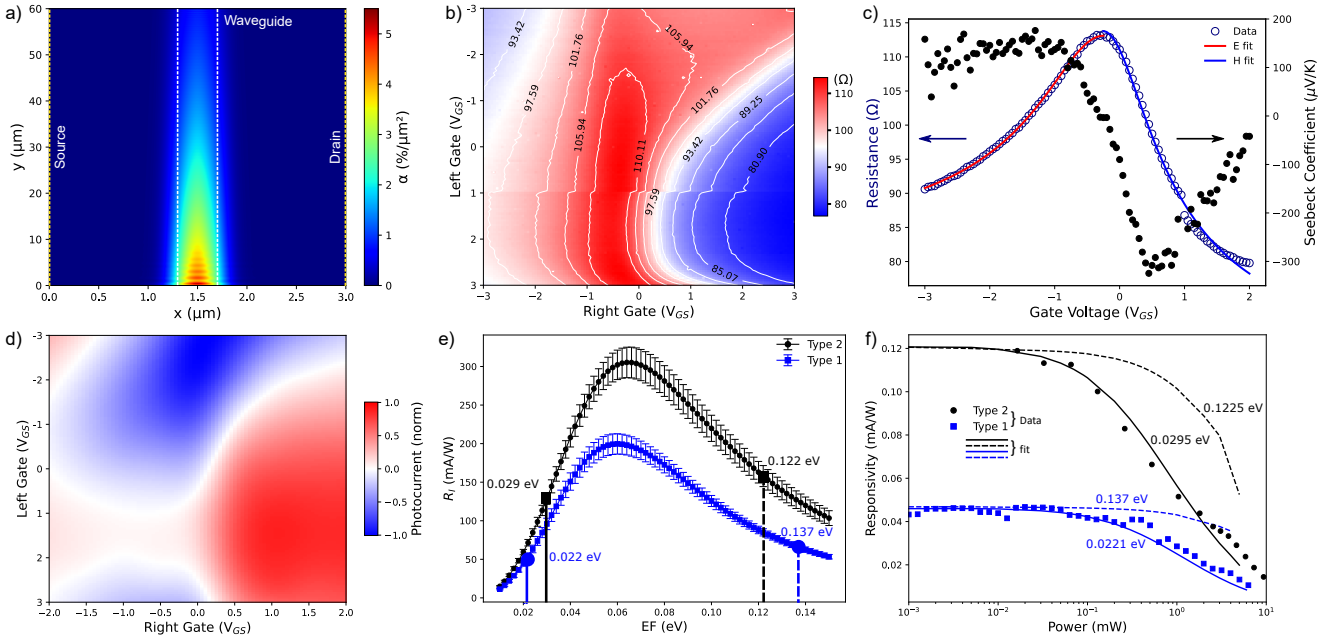


Figure 3: Electrical and optoelectronic characterization of graphene heterostructure PDs. **a** Optical (FDTD) simulation of the photodetector, illustrating the device geometry and absorption-density profile in graphene. **b** Resistance map obtained by sweeping the left and right gate voltages (V_{LG} and V_{RG}); the characteristic p-n pattern peaks at $\sim 112 \Omega$. **c** Resistance as a function of gate voltage for $V_{LG} = V_{RG}$, along with the extracted Seebeck coefficient (S). **d** Photocurrent map at zero bias as a function of V_{LG} and V_{RG} , showing the characteristic sixfold pattern of PTE photodetection and locating the operating gate voltage (OGV). **e** Simulated responsivity vs. E_F along the antisymmetric-gating configurations ($V_{LG} = -V_{RG}$) for Type 1 (blue) and Type 2 (black). Both peak at $E_F \approx 0.07$ eV. Solid vertical lines: operating E_F (Type 1: 0.022 eV; Type 2: 0.029 eV) on the lower- E_F branch. Dashed vertical lines: matched- R_I points on the high- E_F branch. Error bars: statistical variation under $\pm 10,000 \text{ cm}^2\text{V}^{-1}\text{s}^{-1}$ and ± 1 ps operation-range spreads of $\mu(E_F)$ and $\tau_c(E_F)$. **f** Power dependence at the OGV for Type 1 and Type 2. Solid: simulation at the operating E_F (lower- E_F branch). Dashed: simulation at the matched- R_I high- E_F branch — same low-power responsivity, distinguishable saturation behaviour. Data follow the solid curves, confirming operation at $E_F \approx 0.022$ eV (Type 1) and 0.029 eV (Type 2).

$R_I^\infty \propto \sqrt{\tau_c/\mu}$ scaling derived in the cooling-length section applies.

The photocurrent map acquired at zero bias by scanning both gate voltages (Fig. 3d) exhibits the characteristic sixfold pattern of PTE photodetection — six alternating-sign lobes in the (V_{LG}, V_{RG}) plane — that identifies PTE as the dominant photogeneration mechanism and locates the OGV. Numerical thermoelectric simulations using the measured (μ, τ_c, n^*) of each heterostructure as inputs (see Methods, Ref.³⁷) predict peak responsivities of ~ 0.2 A/W (Type 1) and ~ 0.3 A/W (Type 2) at $E_F \approx 0.07$ eV along the antisymmetric-gating configurations $V_{LG} = -V_{RG}$ (Fig. 3e); error bars reflect the standard deviation under the $\pm 10,000 \text{ cm}^2\text{V}^{-1}\text{s}^{-1}$ and ± 1 ps measurement uncertainties on μ and τ_c , respectively. These peak values are at the model-optimum $E_F \approx 0.07$ eV; the OGV operating point is identified separately below.

Power-dependence measurements at zero bias (Fig. 3f) yield low-power responsivities of ~ 0.045 A/W (Type 1) and ~ 0.12 A/W (Type 2), after accounting for input-path optical losses (see Methods). Two gate-voltage configurations consistent with these low-power values exist for each device: one on the lower- E_F side and one on the higher- E_F side of the simulated $R_I(E_F)$ peak (Fig. 3e). The two candidates have distinguishable saturation behaviour at higher power — a consequence of the Fermi-Dirac broadening of $\sigma(E_F, T_e)$ (see Methods). The measured power dependence follows the lower- E_F branch (Fig. 3f, solid lines), identifying the OGV at $E_F \approx 0.022$ eV (Type 1) and $E_F \approx 0.029$ eV (Type 2). Crucially, Type 2 exceeds Type 1 in measured responsivity despite its (relatively) lower mobility — consistent with the ordering predicted by the $R_I^\infty \propto \sqrt{\tau_c/\mu}$ scaling derived above, with magnitudes reproduced by the full numerical model at the OGV (Fig. 3f). The C-band responsivity of the Type 2 device exceeds that of previously reported PTE-based top-illuminated or planar-waveguide graphene PDs^{24,26,31–36,58}, and is comparable to ring-resonator-based PDs (which inherently sacrifice bandwidth³⁵). The Johnson-limited noise-equivalent power (NEP) ranges from $\sim 3.4 \times 10^{-10} \text{ W Hz}^{-1/2}$ at the OGV to $\sim 1 \times 10^{-10} \text{ W Hz}^{-1/2}$ in the linear power range.

High-speed photoresponse and data detection

Next, we investigated the optoelectronic bandwidth of the Type 2 PD to assess the speed of the fabricated waveguide-integrated device. Two distinct setups (See Supp. Note 4) were used. First, a vector-network analyzer (VNA) was employed, with one port connected to a lithium–niobate Mach–Zehnder modulator (MZM) to modulate a CW laser source up to 67 GHz. The output of the MZM was coupled to the device via vertical coupling between a single-mode fiber (SMF) and an on-chip grating coupler (GC). The data points in the green-shaded region of Fig. 4a represent the measured frequency response of the PD (denoted VNA). The data exhibit a flat response up to 65 GHz with no measurable roll-off. The observed signal drop at > 65 GHz is attributed to the bandwidth limitation of the VNA. To measure beyond this range, we used an optical heterodyne setup consisting of a dual-wavelength (DW) frequency-locked laser source with tunable frequency spacing. This source was generated using a lithium–niobate phase modulator (PM) with a 40 GHz bandwidth, driven by a tunable frequency synthesizer⁵⁹. An optical programmable filter was then used to select two comb lines separated by the beat frequency f_{beating} ⁵⁹. We swept f_{beating} in the W-band (75 GHz to 110 GHz) with 5 GHz steps³⁶. Prior to the measurement, a commercial fast PD (Finisar XPDV4120R, denoted cPD) was used to calibrate the setup (See Supp. Note 5). The blue-shaded region in Fig. 4a illustrates the frequency response of the graphene PD up to 110 GHz after calibration and shows no roll-off within the measured range (setup-limited). Although contact resistance contributes to the frequency response, the absence of roll-off up to 110 GHz indicates that hot-carrier dynamics do not limit the bandwidth.

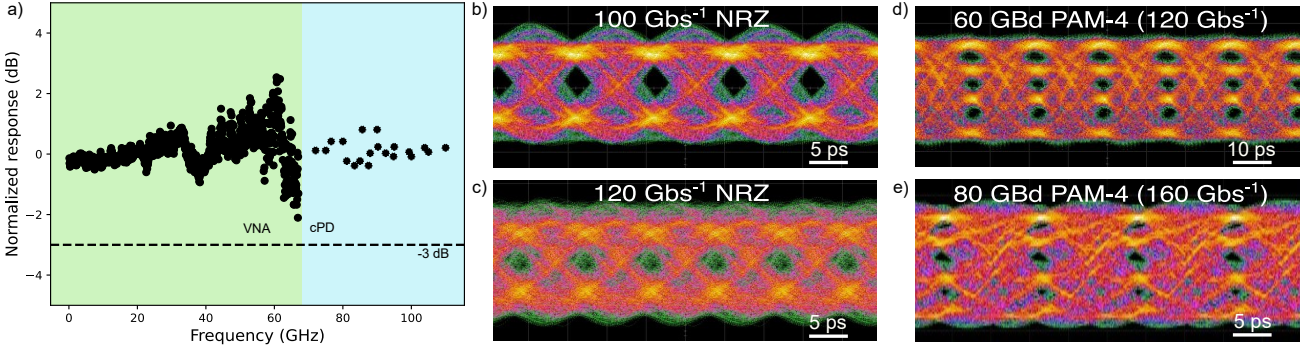


Figure 4: Frequency response of the PD measured with two complementary techniques: VNA (green-shaded region, up to 65 GHz, set-up-limited) and dual-wavelength heterodyne (blue-shaded region, 75–110 GHz). The black dotted line indicates the -3 dB guideline. The Type 2 PD shows no detectable roll-off up to 110 GHz. **b** and **c** Measured eye diagrams at 100 and 120 Gbs⁻¹ using NRZ modulation. **d** and **e** Eye diagrams measured using PAM-4 at 60 and 80 GBd (120 and 160 Gbs⁻¹, respectively).

Subsequently, data detection was performed using two distinct approaches. A 256 GS/s arbitrary waveform generator (AWG) (Keysight M8199B) was used to encode a pseudorandom binary sequence (PRBS) into non-return-to-zero on-off keying (NRZ OOK) and four-level pulse-amplitude modulation (PAM-4). The generated electrical signal was used to drive a lithium–niobate amplitude modulator with a 40 GHz bandwidth, which in turn modulated a continuous-wave (CW) laser source. The signal was then coupled to the PD, and the acquired sequence was subsequently amplified and processed using standard filters such as a continuous-time linear equalizer (CTLE) and a feed-forward equalizer (FFE - 9 taps), both of which were implemented within the oscilloscope software. Fig. 4b and Fig. 4c show the eye diagrams obtained using the NRZ OOK technique, displaying a clear eye opening at 100 Gbs⁻¹ and 120 Gbs⁻¹. From these diagrams, the signal-to-noise ratio (SNR) and bit error rate (BER) were extracted, at 100 Gbs⁻¹: SNR ~ 4.37 , BER $\sim 6.17 \times 10^{-6}$; at 120 Gbs⁻¹: SNR ~ 2.62 dB, BER $\sim 4.35 \times 10^{-3}$, respectively.

Eye closure at high bit rates is limited by the modulator and RF probe bandwidth. Fig. 4d and Fig. 4e present eye diagrams for the PAM-4 modulation at 60 and 80 GBaud, respectively, corresponding to a bit rate of 160 Gbs⁻¹. With a linear filter, we obtain a BER of $\sim 2.3 \times 10^{-3}$ and $\sim 6.7 \times 10^{-3}$, respectively. These values represent a lower bound owing to the setup bandwidth limitation but it is still below the soft decision FEC (SD-FEC) threshold. To the best of our knowledge, this is the highest bit rate achieved by any graphene-based direct receiver at C-band. On the other hand, Type 1 exhibited a data rate of up to 64 Gbs⁻¹ and 128 Gbs⁻¹ using NRZ OOK and PAM-4 modulation (See Supp. Note 5), with corresponding BER of 2.93×10^{-3} and 4.06×10^{-2} as the eye diagram began to close, mainly limited by the setup bandwidth and responsivity. The device also supports higher-order modulation: PAM-8 eye diagrams at 16 and 32 GBaud (48 and 96 Gbs⁻¹) are presented in Supp. Fig. 13d,e, demonstrating compatibility with advanced modulation formats relevant to future 200 Gbs⁻¹-per-lane standards (IEEE 802.3dj). Notably, at 100 Gbs⁻¹ NRZ, the BER of 6.17×10^{-6} is well below the hard-decision forward error correction (HD-FEC) threshold of 3.8×10^{-3} specified by IEEE 802.3 for 100GBASE-LR4 and 100G/400G Ethernet (Supp. Fig. 13b), indicating substantial margin at this data rate. These results place the

Type 2 device in a distinctive operating regime: it converts $\sim 10 \mu\text{W}$ of received optical power into a 160 Gbs^{-1} data stream at an optical energy cost of $\sim 0.06 \text{ fJ/bit}$, with zero energy consumed at the detector and using only linear equalization—without recourse to complex digital signal processing.

Discussion

To identify pathways toward the upper limit of the Type 2 PD’s responsivity, we performed simulations under varying conditions using parameters extracted from our heterostructure, with the experimental configuration (black solid line in Fig. 5a) serving as the reference. Optimizing the p–n junction width and the scalable thickness of the dielectric layer and encapsulant (See Supp. Note 6) increases absorption by 72%, yielding a responsivity of $\sim 0.4 \text{ A/W}$. Overall, Fig. 5a identifies potential pathways for further improving responsivity. To assess how close the simulated responsivities are to the upper bound, we benchmark them against the closed-form framework — extending the asymmetric-contact derivation of Ref. ³⁷ to handle finite-width illumination via a reduction functional $F[a]$ (see Methods):

$$R_I = R_I^\infty \cdot F[a] \cdot \left(1 - e^{-L/\psi}\right) \quad (1)$$

where $R_I^\infty = gS/\beta$ is the ideal current responsivity of Ref. ³⁷ in the long-channel limit ($L \gg \psi$) under δ -function illumination, with $\beta = \sqrt{c_e \kappa_e / \tau_c}$ the heat-exchange coefficient introduced in Ref. ³⁷. $F[a]$ is a reduction functional accounting for the finite width and shape of the illumination profile $a(x)$, derived in this work; for the most relevant case of a Gaussian with FWHM equal to the waveguide width w ,

$$F[a] = F(A) = e^{A^2} \cdot \text{erfc}(A), \quad A = \frac{w}{4\sqrt{\ln 2} \xi},$$

with $\xi = \sqrt{\kappa_e \tau_c / c_e}$ the cooling length. The functional recovers the δ -like limit $F \rightarrow 1$ for $w \ll \xi$ (maximum responsivity) and scales as $F \propto \xi/w$ for $w \gg \xi$ (diminishing response).

Evaluated with the Type 2 parameters at peak- E_F , the analytical current responsivity reaches $R_I^\infty \approx 0.9 \text{ A/W}$ in the δ -function limit, while the Gaussian waveguide profile reduces this to $\approx 0.75 \text{ A/W}$ through $F(A) < 1$ — a $\sim 16\%$ penalty that is purely geometric, arising from the ratio w/ξ between the optical-mode width and the cooling length. In Fig. 5a, the two analytical bounds appear as the dash-dot (δ) and dotted (Gaussian) black lines (Eq. (1) in the $L \gg \psi$ limit, 100% absorption); the solid and dashed curves are the numerical simulations (Methods³⁷). All four come from the same measured (μ, τ_c, n^*) of Type 2. Scaled to matched 72% absorption, the analytical Gaussian bound becomes $\sim 0.54 \text{ A/W}$; the residual $\sim 0.14 \text{ A/W}$ gap to the numerical ($\sim 0.4 \text{ A/W}$) reflects approximations specific to the closed form — strict low-power linearisation, step-function Seebeck profile at the junction, separation of variables, and the $W \gg \xi$ assumption that allows T_e to fully relax at the source–drain contacts. The $W \gg \xi$ requirement is the structural challenge for high- ξ heterostructures, most cleanly addressed by reducing R_C so W can scale with ξ without penalizing bandwidth or current responsivity. The dominant gap from device to unmatched-absorption bound is therefore in-waveguide absorption; the hot-carrier physics established in Fig. 2 is operative throughout.

The headroom identified in Fig. 5a from $\sim 0.3 \text{ A/W}$ (as-fabricated, $\sim 60\%$ absorption) to $\sim 0.4 \text{ A/W}$ (optimised, $\sim 72\%$ absorption) toward $\sim 0.75 \text{ A/W}$ (analytical Gaussian, 100%) and $\sim 0.9 \text{ A/W}$ (analytical δ , 100%) is set primarily by in-waveguide absorption, with the residual closed by reducing the contact-resistance penalty on W . Throughout, the hot-carrier physics established in Fig. 2 is the enabling physics, not the limiting one. Fig. 5b benchmarks our device against reported zero-bias graphene PDs. Prior devices combine bandwidths below 110 GHz with responsivities below $\sim 0.08 \text{ A/W}$ (at OGV); our Type 2 device accesses a previously inaccessible regime at 0.12 A/W and $> 110 \text{ GHz}$, enabling 160 Gbs^{-1} direct detection (Fig. 5c). As mentioned earlier, both Ge-on-Si and III–V UTC photodiodes outperform our device in responsivity by 3–8 \times ; however, this gap is dominated by in-waveguide absorption (currently $\sim 60\%$) rather than by the PTE mechanism itself, and the optimization pathway in Fig. 5a projects $\sim 0.4 \text{ A/W}$ through heterostructure design alone (Supplementary Figs. 15–17). Unlike these technologies^{8,10,11,60}, the PTE mechanism generates a voltage output directly via the Seebeck effect, eliminating the need of TIA. The flat S21 response to 110 GHz —with no observable RC roll-off—implies an effective device capacitance well below the geometric value, consistent with thermal localisation of the active region at high modulation frequencies. For a 160 Gbs^{-1} PAM-4 link (80 Gbaud , requiring 60 GHz system bandwidth), a co-designed voltage amplifier matched to this low capacitance is projected to consume significantly less power ($\sim 0.09 \text{ pJ/bit}$) than a TIA driving a reverse-biased Ge photodiode of comparable bandwidth^{8,12}. Among other 2D materials, waveguide-integrated MoTe_2 ⁶¹ and BP/ MoTe_2 heterojunctions⁶² offer comparable responsivities ($0.4\text{--}0.7 \text{ A/W}$) but remain confined to GHz-range bandwidths.

We note that the $R_I^\infty \propto \sqrt{\tau_c/\mu}$ scaling derived above is specific to the contact-resistance-dominated regime ($R_C/R_G \approx 5$ at the OGV for our Type 2 PD). In a balanced regime $R_C \sim R_G$, the device conductance acquires a μ -dependence and the scaling interpolates toward $\sqrt{\mu\tau_c}$ - a crossover that modulates the relative weight of μ and τ_c in the responsivity, although $\beta \propto \sqrt{\mu}$ persists in both regimes. The relative ordering of heterostructures

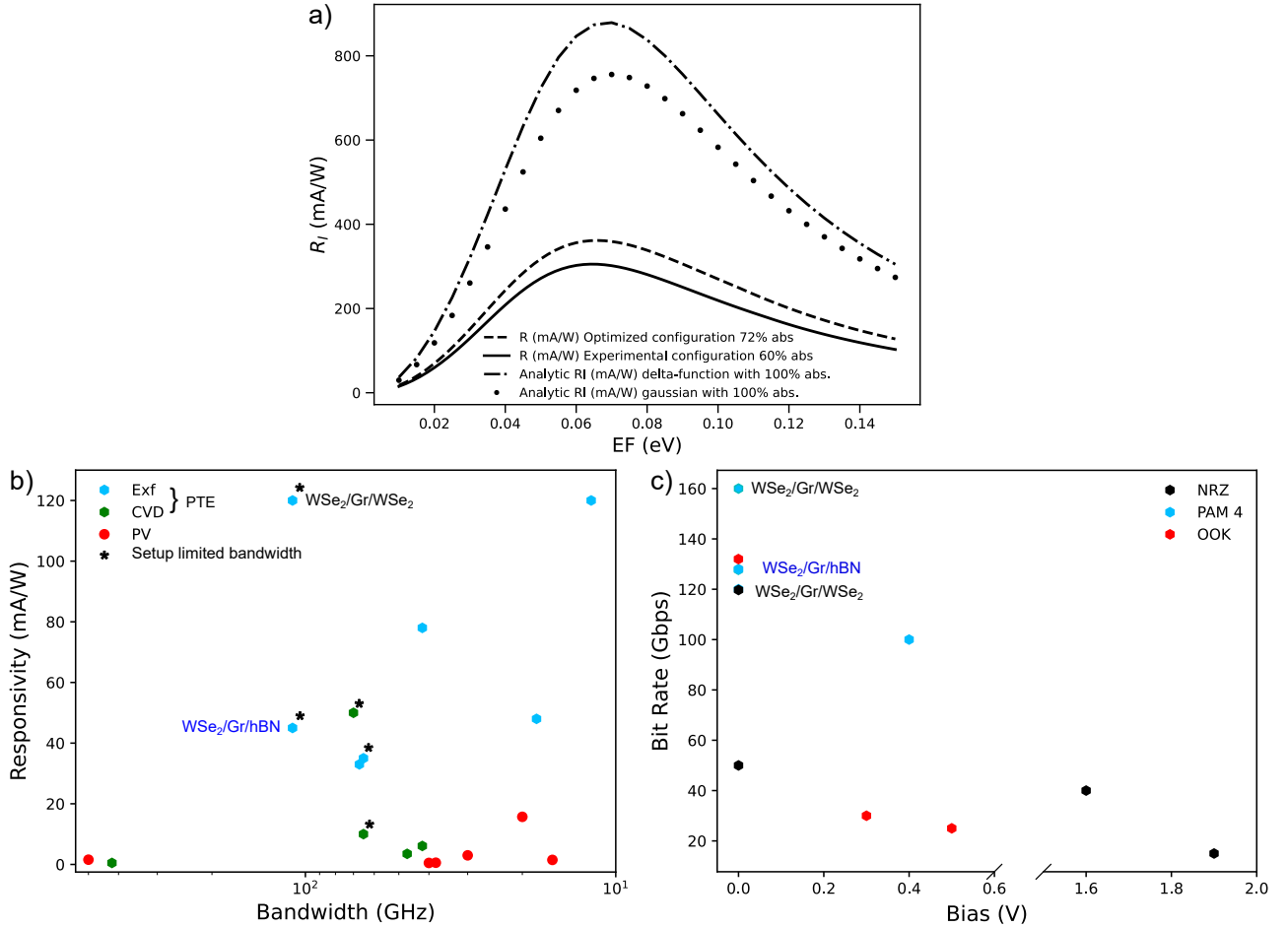


Figure 5: Optimisation and benchmarking of Type 2 photodetectors. **a** Simulated $R_I(E_F)$ for Type 2, evaluated at the measured (μ, τ_c, n^*) ; all curves peak at $E_F \approx 0.07$ eV. Solid: as-fabricated ($\sim 60\%$ absorption, numerical). Dashed: optimised ($\sim 72\%$ absorption, numerical). Dash-dot: analytical δ bound (100% absorption, Methods). Dotted: analytical Gaussian bound (100% absorption, this work, Methods). **b** Comparison of responsivity vs bandwidth for reported zero-bias graphene PDs operating in the C band. Asterisks "*" next to the dataset represent the setup-limited bandwidth. **c** Comparison of the maximum experimentally demonstrated data rates reported for waveguide-integrated graphene-based direct optical receivers. The Type 2 device presented in this work achieves one of the highest reported data rates among graphene-based direct photodetectors.

with different (μ, τ_c, n^*) combinations is therefore regime-dependent, and the optimum stack for a different contact regime would be selected by re-evaluating the framework with the corresponding R_C . The dielectric-environment handle on τ_c therefore remains operative across both regimes; what changes with R_C/R_G is the quantitative weight between τ_c and μ in the responsivity hierarchy.

In summary, we demonstrate that engineering the dielectric environment of graphene—rather than maximising carrier mobility—provides an effective route to break the responsivity–bandwidth trade-off in zero-bias photothermoelectric photodetectors. WSe_2 encapsulation suppresses hot-carrier cooling, reducing the heat-exchange coefficient β and yielding responsivities up to ~ 0.12 A/W with no observable bandwidth roll-off to 110 GHz, enabling direct detection at 160 Gb/s $^{-1}$ (PAM-4). These results establish dielectric control of β as a design axis complementary to mobility and absorption, and show that device optimisation in the PTE regime requires balancing electronic quality against cooling dynamics. The compatibility of WSe_2 with scalable growth^{63–66} and CMOS back-end-of-line integration^{67,68}, combined with zero-bias operation and the elimination of a transimpedance amplifier, positions this platform to address the energy and density constraints of next-generation optical interconnects.

Methods

DC Measurements

Four-probe transport measurements of the Hall-bar devices were performed by applying a low-bias (5–10 mV) between the source and drain electrodes. The resulting voltage drop was measured across the voltage probes using

a lock-in. Two-probe photocurrent measurements of the sSNOM PDs were performed by applying a low-bias voltage (5–10 mV) across the device, with the resulting current change simultaneously recorded using a Keithley source-measure unit. An additional Keithley was used to apply the gate voltage and perform gate sweeps.

Responsivity and NEP calculation

The optical losses in the device were quantified by defining L_1 , L_2 , and L_{dev} as the losses in the regions between the input and the PD, between the PD and the output, and within the PD itself, respectively. The total insertion loss was first measured as $10 \log_{10}(P_{\text{out}}/P_{\text{in}})$ by coupling light into the input and collecting it at the output. This total loss can be expressed as the sum of the individual contributions, $L_1 + L_{\text{dev}} + L_2$. To verify symmetry, the measurement was repeated with the propagation direction reversed (output to input), yielding identical total loss and confirming that $L_1 = L_2$. Under this condition, the total loss reduces to $2L_1 + L_{\text{dev}}$, allowing L_1 to be extracted as $(\text{Total loss} - L_{\text{dev}})/2$. The optical power incident on the detector was then determined as $P_{\text{in}} - L_1$, where P_{in} corresponds to the optical power at the fiber output after accounting for insertion and coupling losses. The responsivity was then calculated as $R = I_{\text{ph}}/(P_{\text{in}} - L_1)$, where I_{ph} is the measured photoresponse and $P_{\text{in}} - L_1$ corresponds to the optical power incident on the PD. The noise current spectral density was estimated from Johnson–Nyquist noise as $i_n = \sqrt{4k_B T/R}$, where R is the device resistance. The corresponding noise-equivalent power was calculated as $\text{NEP} = i_n/|R|$, where R is the responsivity of the device. This expression represents the Johnson-noise-limited NEP.

Optical simulations

Optical simulations were performed using the finite-difference time-domain (FDTD) method (Lumerical), with the numerical setup, mesh refinement, boundary conditions and material parameters for Au, hBN, Si and SiO_2 at $\lambda = 1550$ nm identical to those described in Ref³⁷ (“Optical Modeling”). For WSe_2 at $\lambda = 1550$ nm — below the optical bandgap, so absorption is negligible and we used a uniaxial dielectric with in-plane refractive index $n_{\perp} = 4.0$ and out-of-plane $n_{\parallel} = 2.656$. Graphene was implemented as a 2D conductive surface using the Kubo formalism³⁷ with $\tau_{\text{opt}} = 200$ fs, following Ref³⁷. The fundamental TE mode of the silicon waveguide provided the excitation. The spatial absorption density $\alpha(x, y)$ in the graphene channel was integrated to yield the total absorption α_{SLG} and served as the optical input to the numerical thermoelectric simulations below.

Numerical thermoelectric simulations

Numerical thermoelectric simulations followed the self-consistent scheme of Ref.³⁷ (“Thermoelectric Modeling”). The FDTD-computed absorption density $\alpha(x, y)$ enters as the local heat source in the steady-state heat-dissipation equation for the electronic temperature T_e ,

$$-\nabla \cdot (\kappa_e \nabla T_e) = -\nabla \Pi \cdot j_q - \tau_c^{-1} c_e (T_e - T_0) + \alpha(x, y) P_{\text{in}}, \quad (3)$$

where κ_e is the electronic thermal conductivity, $\Pi = S T_e$ is the Peltier coefficient, $j_q = -\sigma \nabla T_e$ is the local thermoelectric current, σ the electrical conductivity, c_e the electronic specific heat, and P_{in} the input optical power. The graphene transport and thermal parameters (σ, S, c_e, κ_e) are evaluated self-consistently as functions of the local E_F and T_e using the closed-form expressions of Ref.³⁷; the lattice temperature is held at $T_0 = 300$ K given the much larger lattice heat capacity. The measured μ, τ_c, n^* and contact resistance ρ_C of each heterostructure serve as experimental inputs. The mobility μ and cooling time τ_c are taken as gate-voltage-operation-range averages (treated as E_F -independent in the simulation); their statistical spreads propagate to the responsivity error bars in Fig. 3e. The resulting T_e distribution is integrated to give the open-circuit photovoltage

$$V_{\text{PTE}} = \frac{1}{L} \iint S \nabla T_e dx dy$$

and the short-circuit photocurrent $I_{\text{PTE}} = V_{\text{PTE}}/R_D$ with $R_D = R_G + R_C$ the total device resistance. External responsivities are $R_{V,\text{ext}} = V_{\text{PTE}}/P_{\text{in}}$ and $R_{I,\text{ext}} = I_{\text{PTE}}/P_{\text{in}}$. This numerical scheme which does not assume a δ -like or Gaussian absorption profile and retains the full E_F, T_e -dependence of all material parameters produces the simulated curves in Fig. 3e and 3f (solid and dotted lines), and the “experimental” and “optimised” configurations in Fig. 5a. The parameter-sweep maps in Figs. 2e and 2f, and the idealised analytical bounds in Fig. 5a, come instead from the closed-form framework described below. As σ, S, c_e, κ_e and α are all recomputed self-consistently at each iteration as functions of the local (E_F, T_e) , the model captures the power dependence explicitly. In particular, the thermal conductivity $\kappa_e = L_0 \sigma T_e$ depends on T_e through both the explicit prefactor and the Fermi–Dirac broadening of $\sigma(E_F, T_e)$: at lower E_F the broadening tail spans the Dirac point, so a rising T_e thermally activates additional carriers and σ, κ_e and β all climb rapidly with optical power, so the responsivity saturates earlier. At higher $E_F, k_B T_e \ll E_F$ throughout the operating range, σ remains nearly T_e -independent, and the

linear regime extends to higher powers. This mechanism explains why two E_F values can give indistinguishable low-power responsivity (Fig. 3e) but visibly diverge in their high-power behaviour (Fig. 3f), providing a diagnostic of the operating Fermi level.

Parameter-sweep maps and bandwidth estimator

The parameter-sweep maps of Fig. 2e and Fig. 2f are obtained directly from the closed-form framework above. Fig. 2e evaluates $R_I^\infty = \frac{gS}{\beta}$ over (μ, τ_c, n^*) with g , S and β each carrying their full μ -dependence through σ , the Mott formula, and $\kappa_e = L_0\sigma T_e^{37}$ so that the upper-bound responsivity of each heterostructure is read off from its measured transport parameters. Fig. 2f evaluates the bandwidth from

$$f_c = (f_{c1}^{-1} + f_{c2}^{-1})^{-1}, \quad f_{c1} = \frac{1}{2\pi R_D C}, \quad f_{c2} = \frac{1}{\tau_c},$$

with $C = 6$ fF from prior device characterisation of similar geometry [35,36]; this estimator is used for comparative purposes rather than as a device-level bandwidth prediction. The hot-carrier term $f_{c2} = \frac{1}{\tau_c}$ enters as the intrinsic PTE speed limit, following the convention of Ref. 37 (set by hot-carrier cooling dynamics rather than by a Lorentzian 3-dB cut-off), while the RC load enters as the standard 3-dB cut-off $f_{c1} = \frac{1}{2\pi R_D C}$. The harmonic combination is the appropriate form for cascaded first-order responses, equivalent to time constants adding: $\frac{1}{f_c} = \tau_c + 2\pi R_D C$. Fig. 2e, 2f are therefore analytical evaluations of the framework above, distinct from the numerical thermoelectric simulations described earlier (which produce Fig. 3e, f and the “experimental” + “optimised” curves in Fig. 5a).

Authors contribution

F.H.L.K., K.-J.T. and K.P.S. conceived the project. K.P.S. and F.H.L.K. designed the devices. K.P.S. fabricated the devices. I.V. and E.L. performed the simulations reported. S.C. assisted with the modeling. M.M, A.M performed the initial simulations. K.P.S. measured and analyzed the Hall bars. L.O., M.C. and K.P.S. measured and analyzed the sSNOM devices. A.M., V.S., S.M.K., L.K. and K.P.S. measured and analyzed the Type 1 and Type 2 photodetectors. K.W. and T.T. synthesized the hBN crystals. S.A.T. synthesized the TMD crystals. T.R. and D.V.T provided the waveguides. E.L., M.R., J.L. and F.H.L.K. supervised the work and discussed the results. K.P.S., A.M., V.S. and F.H.L.K. wrote the manuscript. All authors contributed to the manuscript revisions. A.M. and I.V. contributed equally to this work.

References

- [1] Cisco Systems, Inc. Cisco annual internet report (2018–2023). White Paper C11-741490-01, Cisco Systems (2020). Cisco Annual Internet Report (2018–2023) White Paper.
- [2] Patrizio, A. Ethernet consortium releases 800gbe spec (2020). Accessed online.
- [3] Cisco Systems, Inc. How to accelerate 400-gigabit ethernet rollout: Optical form factor convergence can support rapid bandwidth expansion. the impact of optics costs on purchases. White Paper, Cisco Systems (2019).
- [4] IEEE 802.3 Working Group. IEEE p802.3dj 200 gb/s, 400 gb/s, 800 gb/s, and 1.6 tb/s ethernet task force (2025). Working Group web page.
- [5] IEEE 802.3 Working Group. IEEE p802.3df task force (2023). Working Group web page.
- [6] Ossieur, P. et al. Integrated photonics and electronics for optical transceivers supporting AI/ML applications. *IEEE Journal of Selected Topics in Quantum Electronics* **31**, 1–16 (2025). Special Issue: AI/ML Integrated Opto.
- [7] IEEE 802.3 Working Group. IEEE p802.3df standard approved! [802.3_B400G] (2023). Email archive announcement.
- [8] Lischke, S. et al. Ultra-fast germanium photodiode with 3-db bandwidth of 265 GHz. *Nature Photonics* **15**, 925–931 (2021).
- [9] Steckler, D., Peczek, A., Kissinger, D., Tillack, B. & Zimmermann, L. Monolithic electro-optic platform on silicon with bandwidth of 100 GHz and beyond. *Nature Communications* **16**, 10467 (2025).
- [10] Li, L. et al. Ultra-fast waveguide MUTC photodiodes over 220 GHz. *arXiv preprint* (2024).
- [11] Li, L. et al. Ultra-fast, high-power MUTC photodiodes with bandwidth-efficiency product over 130 GHz \times 100%. *arXiv preprint* (2025).
- [12] Roelkens, G. et al. Present and future of micro-transfer printing for heterogeneous photonic integrated circuits. *APL Photonics* **9**, 010901 (2024).
- [13] Castro Neto, A. H., Guinea, F., Peres, N. M. R., Novoselov, K. S. & Geim, A. K. The electronic properties of graphene. *Reviews of Modern Physics* **81**, 109–162 (2009).
- [14] Novoselov, K. S. et al. Electric field effect in atomically thin carbon films. *Science* **306**, 666–669 (2004).
- [15] Kuzmenko, A. B., van Heumen, E., Carbone, F. & van der Marel, D. Universal optical conductance of graphite. *Physical Review Letters* **100**, 117401 (2008).
- [16] Nair, R. R. et al. Fine structure constant defines visual transparency of graphene. *Science* **320**, 1308 (2008).
- [17] Jang, C. et al. Tuning the effective fine structure constant in graphene: Opposing effects of dielectric screening on short- and long-range potential scattering. *Physical Review Letters* **101**, 146805 (2008).
- [18] Bolotin, K. I. et al. Ultrahigh electron mobility in suspended graphene. *Solid State Communications* **146**, 351–355 (2008).
- [19] Neumaier, D., Pindl, S. & Lemme, M. C. Integrating graphene into semiconductor fabrication lines. *Nature Materials* **18**, 525–529 (2019).
- [20] Agarwal, H. et al. Ultra-broadband photoconductivity in twisted graphene heterostructures with large responsivity. *Nature Photonics* **17**, 1047–1053 (2023).
- [21] Mak, K. F., Ju, L., Wang, F. & Heinz, T. F. Optical spectroscopy of graphene: From the far infrared to the ultraviolet. *Solid State Communications* **152**, 1341–1349 (2012).
- [22] Soundarapandian, K. P. et al. High-speed graphene-based sub-terahertz receivers enabling wireless communications for 6G and beyond. *Nature Communications* **17**, 2627 (2026).
- [23] Ma, Z. et al. Compact graphene plasmonic slot photodetector on silicon-on-insulator with high responsivity. *ACS Photonics* **7**, 932–940 (2020).

- [24] Shiue, R.-J. et al. High-responsivity graphene–boron nitride photodetector and autocorrelator in a silicon photonic integrated circuit. *Nano Letters* **15**, 7288–7293 (2015).
- [25] Ding, Y. et al. Ultra-compact integrated graphene plasmonic photodetector with bandwidth above 110 GHz. *Nanophotonics* **9**, 317–325 (2020).
- [26] Ma, P. et al. Plasmonically enhanced graphene photodetector featuring 100 gbit/s data reception, high responsivity, and compact size. *ACS Photonics* **6**, 154–161 (2019).
- [27] Guo, J. et al. High-performance silicon–graphene hybrid plasmonic waveguide photodetectors beyond 1.55 μm . *Light: Science & Applications* **9**, 1–10 (2020).
- [28] Liu, C. et al. Silicon/2d-material photodetectors: From near-infrared to mid-infrared. *Light: Science & Applications* **10**, 123 (2021).
- [29] Koepfli, S. M. et al. Metamaterial graphene photodetector with bandwidth exceeding 500 gigahertz. *Science* **380**, 1169–1174 (2023).
- [30] Gabor, N. M. et al. Hot carrier–assisted intrinsic photoresponse in graphene. *Science* **343**, 1016–1020 (2014).
- [31] Muench, J. E. et al. Waveguide-integrated, plasmonic enhanced graphene photodetectors. *Nano Letters* **19**, 7632–7644 (2019).
- [32] Mišeikis, V. et al. Ultrafast, zero-bias graphene photodetectors with polymeric gate dielectric on passive photonic waveguides. *ACS Nano* **14**, 11190–11204 (2020).
- [33] Yu, L. et al. High-bandwidth zero-biased waveguide-integrated p–n homojunction graphene photodetectors on silicon for a wavelength band of 1.55 μm and beyond. *ACS Photonics* (2023). Early access.
- [34] Wang, J. et al. High-responsivity graphene-on-silicon slot waveguide photodetectors. *Nanoscale* **8**, 13206–13211 (2016).
- [35] Schuler, S. et al. High-responsivity graphene photodetectors integrated on silicon microring resonators. *Nature Communications* **12**, 1–10 (2021).
- [36] Marconi, S. et al. Photothermal-effect graphene detector featuring 105 Gbit/s NRZ and 120 Gbit/s PAM4 direct detection. *Nature Communications* **12**, 1–8 (2021).
- [37] Vangelidis, I. et al. Unbiased plasmonic-assisted integrated graphene photodetectors. *ACS Photonics* **9**, 1992–2007 (2022).
- [38] Schuler, S. & Co-authors. Controlled generation of a p–n junction in a waveguide-integrated graphene photodetector. *Nano Letters* **16**, 7107–7112 (2016).
- [39] Alfaraj, N. & Helmy, A. S. Silicon-integrated next-generation plasmonic devices for energy-efficient semiconductor applications. *arXiv* (2025). Preprint.
- [40] Song, J. C. W., Rudner, M. S., Marcus, C. M. & Levitov, L. S. Hot carrier transport and photocurrent response in graphene. *Nano Letters* **11**, 4688–4692 (2011).
- [41] Ma, Q., Andersen, T. I., Nair, N., Gabor, N. M. et al. Competing channels for hot-electron cooling in graphene. *Physical Review Letters* **112**, 247401 (2014).
- [42] Yoshioka, K., Virgilio, B., Kato, T. et al. Ultrafast intrinsic optical-to-electrical conversion dynamics in a graphene photodetector. *Nature Photonics* **16**, 718–723 (2022).
- [43] Purdie, D. G. et al. Cleaning interfaces in layered materials heterostructures. *Nature Communications* **9**, 1–12 (2018). Publisher: Nature Publishing Group. eprint: 1803.00912.
- [44] Wang, W. et al. Clean assembly of van der Waals heterostructures using silicon nitride membranes. *Nature Electronics* (2023). Publisher: Nature Publishing Group.
- [45] Huang, Z. et al. Versatile construction of van der Waals heterostructures using a dual-function polymeric film. *Nature Communications* **2020 11:1** **11**, 1–10 (2020). Publisher: Nature Publishing Group.
- [46] Pogna, E. A. A. et al. Hot-carrier cooling in high-quality graphene is intrinsically limited by optical phonons. *ACS Nano* **15**, 11285–11295 (2021).

- [47] Couto, N. J. et al. Random strain fluctuations as dominant disorder source for high-quality on-substrate graphene devices. *Physical Review X* **4**, 041019 (2014). Publisher: American Physical Society .eprint: 1401.5356.
- [48] Soundarapandian, K. P. et al. Hysteresis-free high mobility graphene encapsulated in tungsten disulfide. *Applied Physics Letters* **123**.
- [49] Kaloni, T. P., Kou, L., Frauenheim, T. & Schwingenschlöggl, U. Quantum spin Hall states in graphene interacting with WS₂ or WSe₂. *Applied Physics Letters* **105**, 233112 (2014).
- [50] Tielrooij, K.-J., Massicotte, M., Otto, M. et al. Out-of-plane heat transfer in van der waals stacks through electron–hyperbolic phonon coupling. *Nature Nanotechnology* **13**, 41–46 (2018).
- [51] Pohl, D. W. Scanning near-field optical microscopy (snom). In Mulvey, T. & Sheppard, C. J. R. (eds.) *Advances in Optical and Electron Microscopy*, vol. 12, 243–312 (Elsevier, 1991).
- [52] Woessner, A. et al. Highly confined low-loss plasmons in graphene–boron nitride heterostructures. *Nature Materials* **14**, 421–425 (2015).
- [53] Betz, A. C. et al. Hot electron cooling by acoustic phonons in graphene. *Phys. Rev. Lett.* **109**, 056805 (2012).
- [54] Graham, M. W., Shi, S.-F., Ralph, D. C., Park, J. & McEuen, P. L. Photocurrent measurements of super-collision cooling in graphene. *Nature Physics* **9**, 103–108 (2013).
- [55] Wang, H. I. et al. Dielectric control of ultrafast carrier dynamics and transport in graphene. *arXiv preprint <https://arxiv.org/abs/2604.00217>* (2026).
- [56] Block, A. et al. Observation of giant and tunable thermal diffusivity of a Dirac fluid at room temperature. *Nature Nanotechnology* **16**, 1195–1200 (2021).
- [57] Ma, Q. et al. Competing channels for hot-electron cooling in graphene. *Physical Review Letters* **112**, 247401 (2014). Publisher: American Physical Society.
- [58] Koepfli, S. M. et al. Controlling photothermoelectric directional photocurrents in graphene with over 400 GHz bandwidth. *Nature Communications* **15**, 7351 (2024).
- [59] Montanaro, A. et al. Sub-thz wireless transmission based on graphene-integrated optoelectronic mixer. *Nature Communications* **14**, 1–8 (2023).
- [60] Sun, K. & Beling, A. High-speed photodetectors for microwave photonics. *Applied Sciences* **9**, 623 (2019).
- [61] Maiti, R. et al. Strain-engineered high-responsivity MoTe₂ photodetector for silicon photonic integrated circuits. *Nature Photonics* **14**, 578–584 (2020).
- [62] Tian, R. et al. Chip-integrated van der Waals PN heterojunction photodetector with low dark current and high responsivity. *Light: Science & Applications* **11**, 101 (2022).
- [63] Kim, K. S. et al. Non-epitaxial single-crystal 2D material growth by geometric confinement. *Nature* **614**, 88–94 (2023).
- [64] Huang, L.-Y. et al. Wafer-Scale Single-Crystal WSe₂ Monolayers Using Substrate-Passivation-Driven Epitaxy. *ACS Nano* **20**, 2104–2113 (2026).
- [65] Xia, Y. et al. Wafer-scale single-crystalline MoSe₂ and WSe₂ monolayers grown by molecular-beam epitaxy at low-temperature — the role of island-substrate interaction and surface steps. *Natural Sciences* **3**, 20220059 (2023). .eprint: <https://onlinelibrary.wiley.com/doi/pdf/10.1002/ntls.20220059>.
- [66] Kwon, J. et al. 200-mm-wafer-scale integration of polycrystalline molybdenum disulfide transistors. *Nature Electronics* **7**, 356–364 (2024).
- [67] Yu, L. et al. High-Performance WSe₂ Complementary Metal Oxide Semiconductor Technology and Integrated Circuits. *Nano Letters* **15**, 4928–4934 (2015).
- [68] Patoary, N. H. et al. Improvements in 2D p-type WSe₂ transistors towards ultimate CMOS scaling. *Scientific Reports* **13**, 3304 (2023).